PHYSICAL REVIEW B VOLUME 49, NUMBER 18 1 MAY 1994-II

Backward-volume-wave microwave-envelope solitons in yttrium iron garnet films

Ming Chen, Mincho A. Tsankov,* Jon M. Nash, and Carl E. Patton
Department of Physics, Colorado State University, Fort Collins, Colorado 80523

(Received 15 November 1993; revised manuscript received 31 January 1994)

Microwave-magnetic-envelope (MME) solitons generated from nonlinear magnetostatic-backward-volume wave packets have been observed in magnetic thin films. The MME signals were excited by 5–50-ns wide microwave pulses at 5.8 GHz in a 15-mm-long by 2.5-mm-wide, 7.2-μm-thick single-crystal yttrium iron garnet (YIG) film strip magnetized in plane and parallel to the long side of the strip. The wave packets were propagated parallel to the static field. The wave packets were launched and the propagating MME pulse signals were detected with planar microstrip transducers 4 mm apart. Envelope soliton behavior was evident from the time-resolved wave forms observed for various input power and pulse width combinations. At low power levels, one sees a relatively broad output pulse which scales with the width of the input pulse and a peak power which increases linearly with the input power. As the input power is increased above some threshold in the 0.5–1-W range, output pulses show a narrowing and steepening which is characteristic of microwave-magnetic-envelope solitons. Further increases in input power produce multiple-peak profiles, characteristic of multiple soliton generation. The experimental results are consistent with the various characteristic times for linear and nonlinear MME pulse propagation and soliton formation. However, numerical modeling based on the magnetic form of the nonlinear Schrödinger equation with initial conditions and parameters which match the experiments yields calculated profiles which show soliton effects but do not quantitatively match the experimental results.

I. INTRODUCTION

Since the early discovery of solitary water waves by Russell,[1] solitons have been observed and studied in many physical systems.[2–5] A well-known example is optical envelope solitons in fibers. Optical solitons have found important applications in telecommunications for long-distance data transmission.[5–10] The term *soliton* usually refers to a propagating pulse or wave packet which preserves its shape without spreading. The manifestations of nonlinear phenomena for such signals as well as applications in communications and signal processing are numerous.[5,9,10]

By far the largest effort concerning solitons has been in the area of nonlinear optics.[5,9,10] In the last decade or so, however, the availability of high-quality, narrow-linewidth single-crystal thin films of yttrium iron garnet (YIG) for microwave signal-processing applications,[11,12] as well as advanced instrumentation for microwave pulse generation, detection, and analysis, has led to a growing interest in microwave-magnetic-envelope (MME) solitons. Such MME solitons have been observed in YIG thin films with various surface pinning conditions and magnetized in different magnetic-field configurations. Both Kalinikos, Kovshikov, and Slavin[13–18] and De Gasperis, Marcelli, and Miccoli[19,20] have studied magnetostatic forward-volume-wave MME solitons in perpendicularly magnetized YIG films with either pinned or unpinned surface conditions. Kalinikos and co-workers[21,22] have also observed surface-wave MME solitons for in-plane-magnetized YIG films with pinned surface spins and pulse propagation perpendicular to the field direction. A new type of MME dark soliton, formed by generating a short 15-ns inverse pulse in a cw microwave carrier at 5.2 GHz in the surface-wave configuration but for films with unpinned surface spins, was obtained recently.[23]

This paper is concerned with the excitation, detection, and analysis of MME solitons generated from nonlinear magnetostatic-backward-volume wave (MSBVW) pulses in in-plane-magnetized thin YIG films with unpinned surface spins and pulse propagation *parallel* to the field direction. In addition to a study of a configuration not previously examined, this work includes a careful experimental study of soliton evolution from the linear-pulse-response regime for two different input-pulse scenarios. In the first, the input power was increased for fixed pulse width. In the second, the pulse width was increased at fixed power. Single-soliton and multiple-soliton responses were observed on both cases. In addition, the resulting profiles of peak output power vs input power and initial pulse width were examined in detail, following the approach of De Gasperis, Marcelli, and Miccoli.[19,20] While these profiles showed the same basic effect reported by De Gasperis, Marcelli, and Miccoli, with an initial nonlinear increase in peak output power as a function of input power due to soliton formation at some critical input power, the present results show that at even higher power levels, the output-signal amplitude *decreases.* Correlation of these data with pulse profiles indicates that the decrease is due to characteristic time effects and multiple-soliton generation. Finally, numerical modeling of soliton profiles based on the magnetic form of the nonlinear Schrödinger equation with boundary conditions and parameters which match the experimental situation yields pulse profiles which show significant discrepancies.

The organization of this paper is as follows: Sec. II provides an overview of the three basic magnetostatic

0163-1829/94/49(18)/12773(18)/$06.00

spin-wave configurations for magnetic thin films, introduces the concept of magnetostatic-backward-volume wave-packet propagation on which the soliton experiments and analyses are based, and presents the four characteristic time parameters important for soliton formation and observation. Section III describes the experimental setup for the measurements and presents several aspects of the YIG film characterization which are critical to both the soliton experiments and the numerical modeling of the results. The experimental results are presented and discussed in Sec. IV. Section V presents theoretical profiles obtained from numerical modeling based on the nonlinear Schrödinger equation.

II. MAGNETOSTATIC-WAVE PULSES IN THIN FILMS

A. Linear magnetostatic waves

The starting point for MME solitons in magnetic thin films is with the magnetostatic waves discussed by Damon and Eshbach.[24] Wave packets for such waves can be generated and detected by microstrip antennas and propagated between antennas with characteristic group velocities, dispersion effects, and decay properties which follow established principles.[11,12] The backward-volume-wave solitons considered in this work derive from magnetostatic-backward-volume wave packets at high power. This section provides a brief introduction to such excitations in the linear regime and additional considerations for the realization of backward-volume-wave MME solitons at high power.

From a classical point of view, magnetic excitations at wave numbers larger than the light wave number at the frequency of interest can be analyzed in terms of the magnetic torque equation and the Maxwell equations under the so-called magnetostatic approximation and with appropriate electromagnetic boundary conditions.[25] The term magnetostatic comes from the fact that the frequency ω_k of the excitation at a given wave number k is well below the corresponding light frequency at the same k value. For thin films and a range of wave number k from about 10^2 to 10^6 rad/cm, these excitations are usually termed magnetostatic waves or dipole-exchange spin waves, depending on the role of the exchange interaction in the analysis.

Magnetostatic waves in ferromagnetic slabs were studied theoretically by Damon and Eshbach[24] for the case of a ferrite slab magnetized to saturation by an in-plane magnetic field. Damon and van de Vaart[26] later considered the case of slabs magnetized perpendicular to the slab plane. These waves and their dispersion characteristics fall into three categories, magnetostatic surface waves (MSSW's) and magnetostatic backward-volume waves (MSBVW's) for the in-plane-magnetized slab case, and magnetostatic forward-volume waves (MSFVW's) for the perpendicularly magnetized slab case.

The three categories of magnetostatic waves are shown schematically in Fig. 1, with sketches showing the field-magnetization-propagation geometry and characteristic dispersion curves in each case. In order to facilitate later connections with the experimental results, the dispersion curves shown in Fig. 1 are actual calculated curves for a prototype thin YIG film with a thickness $S=7.2$ μm, a saturation induction $4\pi M_s=1750$ G, and a gyromagnetic ratio $\gamma=2.8$ GHz/kOe. All curves are for an effective net internal static magnetic field H of 1407 Oe, in order to give dispersion curves which quantitatively match the experimental conditions for the MSBVW experiments. The connection between H and the applied static field H_{app} for the experiments is discussed in Sec. III. Three characteristic frequencies, ω_B, ω_S, and ω_H, are indicated in the diagrams. These frequencies define the magnetostatic-wave (MSW) band limits discussed below. The schematic wave packet inset in the middle diagram denotes a propagating 5.8-GHz MSBVW wave packet which will be the focus of the experiments. The choice of frequencies and fields for the MSBVW experiments is discussed in detail in Sec. III.

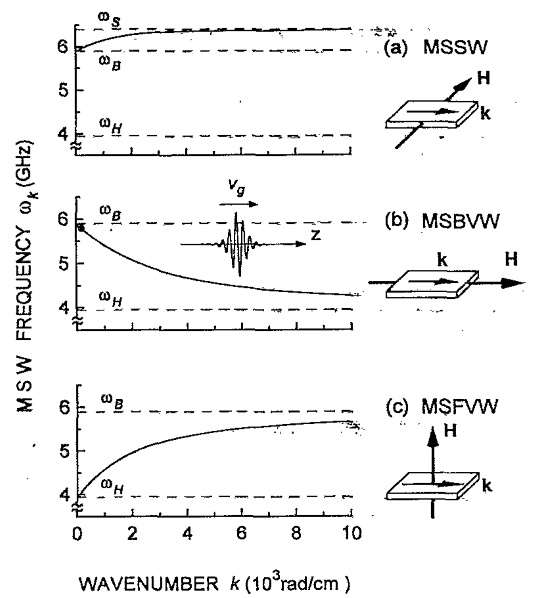

FIG. 1. Dispersion diagrams of magnetostatic wave frequency ω_k vs wave number k for the three basic thin-film magnetostatic wave configurations, (a) magnetostatic surface waves (MSSW), (b) magnetostatic-backward-volume waves (MSBVW), and (c) magnetostatic-forward-volume waves (MSFVW). The relative orientations of the net static field **H** and the wave vector **k** to each other and to the film for each configuration are shown by the diagrams to the right of the dispersion diagrams. The horizontal dashed lines and the frequencies ω_S, ω_B, and ω_H denote band limits for the different configurations. The curves are actual calculated curves from magnetostatic wave theory for a 7.2-μm-thick yttrium iron garnet film with $H=1407$ Oe. The filled circle at 5.8 GHz on the middle MSBVW curve denotes the operating point for the soliton experiments. The wave-packet diagram inset on the middle graph denotes a MSBVW pulse traveling at a velocity v_g.

Figure 1(a) shows the surface wave (MSSW) case for an in-plane-magnetized film with the wave vector **k** *perpendicular* to the in-plane field **H** and the saturation magnetization $\mathbf{M}_s$. The surface-wave dispersion curve starts out at a characteristic frequency ω_B at $k=0$. For the parameters indicated above, ω_B is at 5.900 GHz. With increasing wave number k, the MSSW frequency increases and asymptotically approaches a second characteristic frequency ω_S for $k \gg 1/S$. For the parameters listed above, the band for MSSW excitations ranges from $\omega_B = 5.900$ GHz up to $\omega_S = 6.390$ GHz. This excitation is called a surface wave because the dynamic magnetization response **m** is localized at the surface of the slab or film for $k \gg 1/S$. Note that this MSSW dispersion curve has a *negative* $\partial^2\omega_k/\partial k^2$ dispersion coefficient. As will be evident shortly, $\partial^2\omega_k/\partial k^2$ is an important parameter for MME solitons. This parameter will be denoted by ω_k''.

Figure 1(b) shows the backward-volume-wave case for an in-plane magnetized film with the wave vector **k** *parallel* to **H** and to $\mathbf{M}_s$. The MSBVW dispersion curve also starts out at ω_B for $k=0$. With increasing k, however, the MSBVW frequency decreases and asymptotically approaches the third characteristic frequency, ω_H, at $k \gg 1/S$. For the parameters listed above, the MSBVW band ranges from ω_B down to $\omega_H = 3.940$ GHz. The backward-volume-wave terminology derives from the negative group-velocity parameter, $v_g = \partial\omega_k/\partial k$, which is evident from the negative slope of the dispersion curve in Fig. 1(b) over the entire band, and a dynamic magnetization response **m** which extends through the thickness of the film. Note that the MSBVW dispersion curve in Fig. 1(b) has a *positive* ω_k'' dispersion coefficient.

The frequencies ω_B and ω_H will turn out to be important parameters in the MSBVW analysis which follows. These frequencies are the same as the bulk spin-wave band limiting frequencies at low k,

$$\omega_B = \gamma[H(H+4\pi M_s)]^{1/2} \tag{1}$$

and

$$\omega_H = \gamma H \ . \tag{2}$$

The upper-limit frequency ω_B can also be expressed as $\omega_B = [\omega_H(\omega_H+\omega_M)]^{1/2}$, where $\omega_M = \gamma 4\pi M_s$ denotes the saturation induction in frequency units.

Figure 1(c) shows the forward-volume-wave case for a perpendicularly magnetized film. In this case, the net external static field is equal to $H + 4\pi M_s$. The MSFVW dispersion curve starts out at ω_H at $k=0$. With increasing k, the MSFVW frequency increases and approaches ω_B at $k \gg 1/S$. The MSFVW band ranges from ω_H up to ω_B. The forward-volume-wave terminology derives from the positive group velocity $v_g = \partial\omega_k/\partial k$, as evident from the positive slope of the dispersion curve in Fig. 1(c) over the entire band, and a dynamic magnetization response **m** which extends through the thickness of the film. Note that the MSFVW dispersion curve in Fig. 1(c) has a *negative* ω_k'' dispersion coefficient.

The curves in Fig. 1 are based purely on the magnetostatic theory, without exchange. While exchange can complicate the dispersion diagrams significantly, the effects are not important in this lead-in discussion for backward-volume waves. For surface waves and forward-volume waves, and particularly for films with pinned surface spins, exchange can lead to important effects for both linear MSW signals and MME solitons. These points are discussed by De Wames and Wolfram,[27,28] Sparks,[29] Kalinikos,[30,31] and Patton.[32]

Magnetostatic-wave pulse propagation is possible for all three configurations shown in Fig. 1, as long as one utilizes a carrier frequency located within the applicable band limits and sufficiently wide pulses to maintain a narrow spectral width. The group velocity of such pulses will be determined by the frequency operating point within the band and the slope of the dispersion curve at that point. For a given propagation distance, as between microstrip transducers, the decay in pulse height due to damping will be smallest for the largest possible group velocity. This condition is accomplished by operating close to the ω_B point for MSSW or MSBVW pulses and to the ω_H point for MSFVW pulses. The filled circle on the MSBVW dispersion curve in Fig. 1(b) at 5.8 GHz indicates such an operating point. The downshift of this operating point from ω_B, by 100 MHz in this case, is needed because of the spectral width in frequency content caused by the finite pulse width. For a pulse width T_0 of 10 ns, the spectral half-width of the microwave pulse signal is $1/T_0 = 100$ MHz.

The wave packet shown in the inset for Fig. 1(b) is intended to represent a propagating MSBVW pulse at the applicable group velocity, $v_g = \partial\omega_k(\mathrm{rad/s})/\partial k(\mathrm{rad/cm})$. Both v_g and the dispersion parameter ω_k'' can be determined empirically from measurements of pulse propagation time vs frequency at low power. Such measurements are described in Sec. III. The empirical values for v_g and ω_k'' obtained in Sec. III for the $\omega_k = \omega = 5.8$ GHz operating point and MSBVW band shown in Fig. 1 are -3.24×10^6 cm/s and 1.41×10^3 cm^2/rad s, respectively. These values are in good agreement with theory. The wave number k at the operating point is about 200 rad/cm. This single operating point will be used for the soliton experiments described in Sec. IV.

As indicated above, low-power MSSW, MSBVW, and MSFVW wave-packet propagation work has been done by numerous workers.[11,12] In addition, MME solitons have been reported for the MSSW and MSFVW configurations and YIG films with both pinned and unpinned surface spins. Until now, however, the MSBVW configuration has not been used to generate MME solitons, to our knowledge. This situation is due to several reasons. First, it is more difficult to realize the MSBVW configuration experimentally because the field is parallel to the propagation direction for the structure. This necessitates a relatively wide magnet gap, problems with microwave connections, field inhomogeneity, etc. Second, the absence of dipole-exchange gaps in this configuration, even for films with pinned surface spins, makes it necessary to use relatively short microwave pulses down to 10 ns or so. For the present experiment, these difficulties have been solved and MSBVW solitons have been generated and detected. The experiment, experimental results, and comparisons with theory are described in the sections which follow. This section is concluded with a brief summary of theoretical considerations for MME solitons.

B. Nonlinear magnetostatic waves and MME solitons

Consider an x-y-z coordinate system for the in-plane-magnetized film as shown in Fig. 2. The x direction is perpendicular to the film. The y direction is in plane. The in-plane z direction is along $\mathbf{k}$, $\mathbf{H}$, and $\mathbf{M}_s$. This configuration matches the setup for MSBVW wave-packet propagation in Fig. 1(b). Figure 2 also shows the magnetization vector $\mathbf{M}$ for some particular point in the sample as a precessing vector with its large and nearly static component along the z direction and the transverse dynamic magnetization, $\mathbf{m}$, as well. For a MSBVW plane wave, the precession cone would remain the same size and only the phase would change as one moves along the z direction. For a wave packet, this plane wave would be modulated by some localized shape function which propagates along the z direction as well. Let the in-plane y component of the transverse dynamic magnetization response be denoted by $m_y(z,t)$. That response may be written as

$$m_y(z,t)=M_s u(z,t)e^{-i(kz-\omega t)} , \tag{3}$$

where $u(z,t)$ is a dimensionless and complex envelope response function for the propagating $m_y(z,t)$ signal, ω is the MSBVW carrier-signal frequency close to the ω_B point in Fig. 1(b), and k is the MSBVW carrier-signal wave number at frequency ω. In the $k=0$, $\omega=\omega_B$ limit, the dynamic magnetization precession response for both ferromagnetic resonance (FMR) and MSBVW signals for in-plane-magnetized films satisfies the condition $|m_x|/|m_y|=\omega_H/\omega_B$.[24] The x-component dynamic magnetization response can then be written as

$$m_x(z,t)=iM_s\frac{\omega_H}{\omega_B}u(z,t)e^{-i(kz-\omega t)} . \tag{4}$$

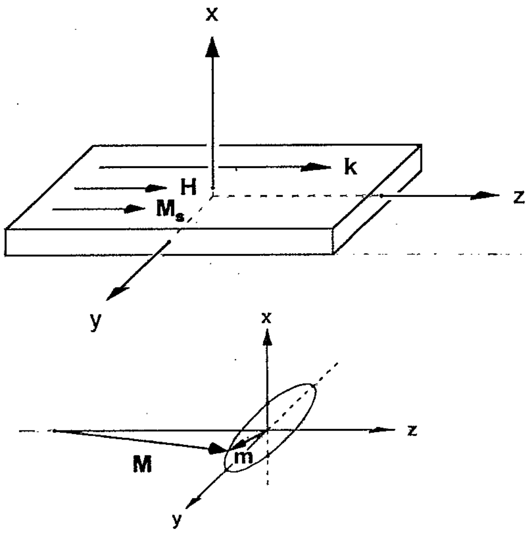

FIG. 2. Coordinate system for the film and dynamic magnetization response for the nonlinear Schrödinger equation analysis. The x axis is perpendicular to the film plane. The y axis is in-plane. The z axis is in plane and parallel to the net static field $\mathbf{H}$, the magnetostatic-backward-volume wave vector $\mathbf{k}$, and the static magnetization $\mathbf{M}_s$. The bottom diagram shows, in schematic form, the magnetization vector $\mathbf{M}$ in precession with the transverse dynamic magnetization $\mathbf{m}$.

The envelope response function $u(z,t)$, as yet unspecified, is taken to have a temporal width T which is sufficiently long to yield a spectral half-width $\Delta\omega=1/T$ which is smaller than $(\omega_B-\omega)$. This constraint is needed to insure that the entire spectral response is within the MSBVW passband. The pulse narrowing which takes place during soliton formation makes this constraint even more important in the nonlinear regime. A small $\Delta\omega$ also ensures that the v_g and ω_k'' parameters defined above and the other parameters defined below for a plane wave, when evaluated at the specific (k,ω) operating point, can be applied to the wave packet. The relevant response parameter for the analysis and discussion will be the *square* of the *magnitude* of $u(z,t)$. In order to distinguish between measured power vs time profiles and calculated $|u|^2$ vs time profiles, etc., the quantity $|u|^2$ will be termed the power amplitude.

Now consider the effect of the above dynamic response on the z component of the magnetization. To lowest order in m_x and m_y, and under the condition that the magnitude of the total magnetization is a constant, $|\mathbf{M}(z,t)|=M_s$, M_z is given by

$$\begin{aligned} M_z &= M_s-\frac{|m_x(z,t)|^2+|m_y(z,t)|^2}{2M_s} \\ &= M_s\left[1-\frac{1}{2}\left[1+\frac{\omega_H^2}{\omega_B^2}\right]|u(z,t)|^2\right] . \end{aligned} \tag{5}$$

Due to the fact that the MME wave packet is a propagating, modulated wave, M_z is not strictly static. However, for a wave packet of many cycles, $M_z=M_z(z,t)$ may be taken as the reduced effective static magnetization at some localized point inside the packet.

Turn now to the matter of solitons. The key factor concerns the effect of wave amplitude on frequency. This effect may be expressed in terms of a nonlinear response parameter N defined by

$$N=\frac{\partial\omega_k}{\partial|u|^2} . \tag{6}$$

This N parameter represents the rate of change in the MSW frequency ω_k with $|u(z,t)|^2$. It is this nonlinear effect which can be used, in certain situations, to compensate for the wave-packet spreading caused by dispersion. From relatively simple arguments based on the net effect of dispersion and power amplitude on carrier frequency,[9] one can show that the pulse narrowing which precedes soliton formation can occur only if the condition

$$\omega_k''N<0 \tag{7}$$

is satisfied. Equation (7) amounts to a condition on the relative directions of the MSW group-velocity shift with respect to wave number k and frequency shift with respect to the power amplitude $|u|^2$. In order for the nonlinear shift due to $|u|^2$ to compensate the shift due to dispersion and allow for soliton formation, these shifts must be in *opposite* directions. The Eq. (7) condition is often referred to as the Lighthill criterion, based on an identical condition obtained by Lighthill[33] for the modulational instability of cw waves in nonlinear dispersive systems. It is also the condition for soliton formation.[6,34,35] From the positive curvature for the MSBVW ω_k vs k dispersion curve in Fig. 1(b), it is clear that ω_k'' is positive. The nonlinear N parameter for MSBVW wave packets with $\omega \approx \omega_B$ is negative. Equation (7) is satisfied for MSBVW wave packets.

For the present case of sufficiently wide MSBVW pulses with a carrier frequency ω which is close to ω_B, the N parameter can be evaluated in a straightforward manner. One first writes ω_B in Eq. (1) in terms of M_z instead of M_s, according to

$$\omega_B(M_z)=\gamma[H(H+4\pi M_z)]^{1/2} . \tag{8}$$

One then takes $\omega_k(M_z)$ to be approximately equal to $\omega_B(M_z)$ and uses the connection between M_z and $|u(z,t)|^2$ in Eq. (5) to evaluate N as $\partial\omega_B/\partial|u(z,t)|^2$. The result of this procedure is

$$N=-\frac{\omega_H\omega_M}{4\omega_B}\left[1+\frac{\omega_H^2}{\omega_B^2}\right] . \tag{9}$$

This result is the same as stated by Zvezdin and Popkov.[36] For the YIG parameters and field value given above, one obtains $N=-7.432\times10^9$ rad/s.

Given the possibility of soliton formation, four characteristic times become important: (1) a characteristic relaxation time T_r, (2) a characteristic dispersion time T_d, (3) a characteristic nonlinear response time T_n, and (4) the propagation time from wave-packet launch to observation T_p. The relaxation time T_r is simply the decay time of the dynamic magnetization response due to energy dissipation. If only relaxation is considered, the amplitude of the MME wave packet will simply decay according to $e^{-\eta t}$ with a characteristic $1/e$ decay time given by

$$T_r=\frac{1}{\eta} . \tag{10}$$

The η parameter is the microwave relaxation rate in rad/s for the applicable (k,ω_k) mode. This relaxation rate for MSBVW signals was determined from low-power attenuation measurements described in Sec. III B. The result is $\eta=7.5\times10^6$ rad/s. This value will be used, where needed, for numerical calculations. This value of η corresponds to an equivalent linewidth of about 0.85 Oe, roughly 2–3 times the expected intrinsic linewidth for single-crystal YIG at 6 GHz. This larger damping is attributed, in part, to the additional losses associated with the interaction of the propagating mode with the YIG film substrate.[37] Based on the above η value, T_r is 113 ns.

The dispersion time T_d may be defined as the time for a pulse of initial width T_0 and power amplitude $|u_0|^2$ to decay to half of its initial power amplitude due to dispersion. One can calculate the decay by assuming that the total energy in the pulse in the absence of relaxation is constant and proportional to $|u(t)|^2T(t)=|u_0|^2T_0$, where $|u(t)|^2$ and $T(t)$ are the time-dependent power amplitude and pulse width. To a good approximation, the dispersion time is given by

$$T_d=\frac{v_g^2T_0^2}{|\omega_k''|} . \tag{11}$$

For the parameters given above, one obtains T_d (ns) $=7.4[T_0\text{ (ns)}]^2$.

The nonlinear response time may be defined as the time for the nonlinear frequency shift to yield a phase change of π between the original low-power carrier signal and the shifted carrier signal at power amplitude $|u_0|^2$. This time is obtained as

$$T_n=\frac{\pi}{|N||u_0|^2} . \tag{12}$$

For the N value given above, one obtains T_n (ns) $=4200/[|u_0|^2\times10^4]$. Note that for T_n to fall in the 100-ns range relevant to the current experiments, the $|u_0|^2\times10^4$ parameter must be on the order of 40. This corresponds to an initial $|m_x|$ response which is about 6% of M_s. Dispersion and nonlinear response times, and expressions equivalent to Eqs. (11) and (12) in the context of nonlinear optics, are discussed by Agrawal.[10]

The fourth characteristic time is the propagation time T_p for the low-amplitude wave-packet pulse in a particular experiment. This time is given simply by

$$T_p=\frac{L}{|v_g|} , \tag{13}$$

where L is the distance between the input and output transducers. Measurements of T_p vs frequency for low-power MSBVW pulses may be used to measure $|v_g|$. In the present experiment, L is 4 mm and T_p is 124 ns at the 5.8-GHz operating point.

The interplay between these various characteristic times sets the conditions for both the linear pulse response at low power and the generation and observation of solitons at high power. In simple terms, the formation of solitons involves a compensation for the phase change between the wave-packet harmonic components caused by dispersion by the phase change caused by the nonlinear frequency shifts for these components. This compensation can occur only if the nonlinear response time T_n is *smaller* than the dispersion time T_d. This condition leads to a minimum value of the product $T_0^2|u_0|^2$ for soliton formation. From Eqs. (11) and (12), the condition $T_n<T_d$ leads to the basic result $T_0^2|u_0|^2>(\pi/|v_g|^2)|\omega_k''/N|$. A rigorous treatment[38] which includes the possibility of the generation of more than one soliton leads to[36]

$$T_0^2|u_0|^2>(n-\tfrac{1}{2})^2\frac{\pi^2}{|v_g|^2}\left|\frac{\omega_k''}{N}\right| , \tag{14}$$

where n is a positive integer soliton number which loosely corresponds to the number of solitons created. This result reflects the intuitive expectation that the *lower* the dispersion or the *higher* the nonlinear frequency response parameter N, the shorter the pulse width and/or the lower the power amplitude needed to produce solitons. The MSW soliton experiments by Kalinikos, Kovshikov, and Slavin[13] took advantage of the large values of the dispersion parameter ω_k'' for the dipole-exchange regions of the dispersion curves for films with pinned surface spins in order to observe soliton behavior with relatively wide pulses at $T_0 \approx 200$ ns or so. The present work is on films with unpinned surface spins, for which the ω_k'' parameter is three orders of magnitude smaller. In this case, Eq. (14) can be satisfied for much shorter pulses, in the 10-ns region. Based on the parameters already indicated, Eq. (14) gives critical $T_0^2|u_0|^2 \times 10^4$ product values for one, two, and three solitons of 447, 4023, and 11 177 ns^2, respectively.

There are additional constraints on $|u_0|^2$ which are related to the relaxation time T_r and the propagation time T_p. Consider relaxation first. The condition $T_n < T_d$ is already imbedded in Eq. (14). However, if the nonlinear response time T_n is *longer* than the relaxation time T_r, decay due to relaxation will dominate and the soliton generation will not be possible. Basically, the pulse decays before it has a chance to form a soliton. A second condition for solitons, therefore, is obtained from $T_n < T_r$. This amounts to a condition on the initial pulse power amplitude $|u_0|^2$ alone.

$$|u_0|^2 > |u_0|_{rn}^2 = \frac{\pi}{|N|}\eta \; . \tag{15}$$

For the values of N and η already given, one obtains $|u_0|_{rn}^2 \times 10^4 = 31.7$.

Now consider the propagation-time constraint. In order to observe solitons which have been completely formed, the propagation time T_p should be *longer* than the nonlinear response time T_n. This amounts to a *second condition* on the initial pulse power amplitude $|u_0|^2$,

$$|u_0|^2 > |u_0|_{pn}^2 = \frac{\pi}{|N|}\frac{|v_g|}{L} \; . \tag{16}$$

For the parameter values already given, one obtains $|u_0|_{pn}^2 \times 10^4 = 34.2$. Equation (16) is essentially the same as Eq. (15), except with a propagation rate $|v_g|/L$ parameter in place of the relaxation frequency η. This means that under conditions for which the propagation time T_p is less than the relaxation time T_r, the propagation frequency $|v_g|/L$ parameter will play the role of η as far as the experimental observations are concerned. In the present case, the relaxation time and the propagation time are comparable, and the $|u_0|_{rn}^2$ and $|u_0|_{pn}^2$ are also comparable.

It is important to realize that none of the above limits represents hard conditions on either the creation or the observation of soliton behavior. Note first that the various characteristic times are defined somewhat arbitrarily, in terms of a $1/e$ decay for T_r, a doubling in pulse width for T_d, and a phase change of π for T_n. Other definitions could have been used as well. The critical product from Eq. (14), therefore, represents more a rule of thumb than a definite threshold for n solitons. The damping and propagation time constraints, moreover, simply mean that whatever behavior is observed may correspond to additional damping effects if Eq. (15) is not satisfied or incomplete soliton formation if Eq. (16) is not satisfied.

One final consideration for MSBVW soliton generation involves the need to avoid spin-wave instability effects. For first-order effects,[25,39] the basic requirement is that the spin-wave-frequency point at $\omega_k = \omega/2$ falls below ω_H. For operation close to the top of the MSBVW band with $\omega \approx \omega_B$, this requirement reduces to the condition $\omega > 2\omega_M/3$. For YIG, $2\omega_M/3$ is 3.27 GHz. The current operating point of 5.8 GHz is well above this limit.

Second-order instability[39,40] is possible under the conditions described above for MSBVW signals and it is important to keep the power amplitude below the threshold for these effects. At FMR, corresponding to an operating point at $\omega = \omega_B$ and $k = 0$, the critical power amplitude for second-order instability could be quite small. Based on the formulas in Ref. 40, the assumption of an in-plane static field, a linearly polarized microwave field perpendicular to the film plane, the usual uniform mode FMR response,[41] and a spin-wave relaxation rate equal to the MSBVW relaxation rate, second-order instability occurs at $|u_0|^2 \times 10^4 \approx 10$. In the present MSBVW experiment at an operating point 100 MHz below the FMR point, this threshold would be a factor of 100 or more larger.

III. TRANSDUCER STRUCTURE AND LINEAR MSW PROPAGATION

This section is concerned with the experimental arrangement for the excitation of linear MSBVW wave packets and MME solitons in YIG films. The experiments were performed at room temperature using a magnetostatic-wave-transducer structure[11,12,15] in the backward-volume-wave configuration at 5.8 GHz. Section III A describes the experimental setup. Section III B gives results on the linear MSBVW wave-packet propagation characteristics for the structure. These results provide a check on the nature of the MSBVW signals under study and yield an empirical determination of two key parameters which play important roles in the characteristic times and the numerical modeling, v_g and ω_k''.

A. Experimental setup

The measurements utilized an epitaxial YIG film and planar microwave-transducer structure. The film was provided by Dr. J. D. Adam, Westinghouse Research and Development Center, Pittsburgh, Pennsylvania. It was grown on a (111)-plane single-crystal gadolinium gallium garnet (GGG) substrate by the method of liquid-phase epitaxy (LPE).[12] The film thickness, based on the LPE processing parameters, was 7.2 μm. The film was characterized by ferromagnetic resonance at 9.5 GHz for both in-plane and perpendicular-to-plane static fields. These FMR spectra, while complicated, were consistent with the magnetic parameters given above, a film in the (111) crystallographic plane, and with a small contribution to the effective static field H due to the cubic magnetocrystalline anisotropy. From low-power cw MSBVW measurements on the actual transducer structure, discussed below, this anisotropy field was set at 64 Oe. A comparison of the FMR spectra with predictions from dipole-exchange mode theory[30] indicates that the surface spins in the film are nearly unpinned. The derivative peak-to-peak linewidths for the low-order magnetostatic modes in the in-plane-field FMR configuration were about 0.35 Oe. These linewidths are consistent with the nominal half-power linewidth of about 0.05 Oe/GHz for single-crystal YIG.[42] Several different long narrow films were used for the MSBVW measurements. The results presented below and in Sec. IV are for one particular 2.5×15 mm^2 rectangular film sample. Similar results were obtained for other samples.

The microwave-transducer structure for the MSBVW measurements consists of two microstrip transducer lines on a RT/duroid® copper-clad microwave dielectric laminate[43] with the rectangular YIG film on top. The structure/film setup is shown schematically in Fig. 3. Standard 50-Ω planar transmission lines are used for input and output. These lines connect to narrow 50-μm-wide, 2.5-mm-long transducer sections which are then shorted to ground. The YIG/GGG rectangle is placed YIG-film-side down across this transducer structure as shown in the figure. The transducer section for the input line serves as a launcher for the MSW signal and the corresponding output section serves as a pickup antenna. The 50-μm width for the transducer sections of the microstrip lines represents a compromise between adequate impedance matching to the magnetic film and good coupling for moderate-k MSW modes. The 50-μm width provided adequate coupling to propagate low-wave-number MSW signals in the $k < 10^3$ rad/cm range. The wavelength for the $k \approx 200$ rad/cm MSBVW signal at the 5.8-GHz operating point in Fig. 1(b) is about 300 μm. The transducers are spaced 4 mm apart. This spacing provides a large enough separation to resolve the 5–50-ns MSW pulses, but still small enough to give reasonable signals at the pickup transducer. The structure was designed for an operating frequency of about 6 GHz.

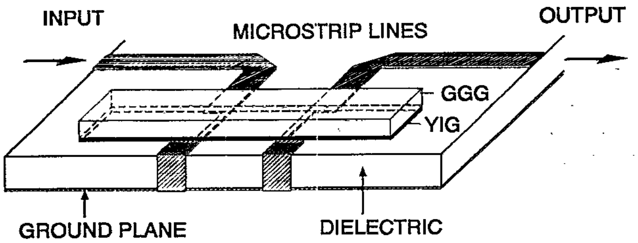

FIG. 3. Diagram of the YIG-film transducer structure. The structure consists of two planar microstrip transmission lines which narrow down to input and output transducer sections. These lines are on the top surface of a RT/duroid® laminate dielectric substrate with a conducting-ground plane backing. The long and narrow YIG film on a gadolinium gallium garnet (GGG) substrate is positioned YIG-side down over the trans-ducer sections of the input and output microstrip lines.

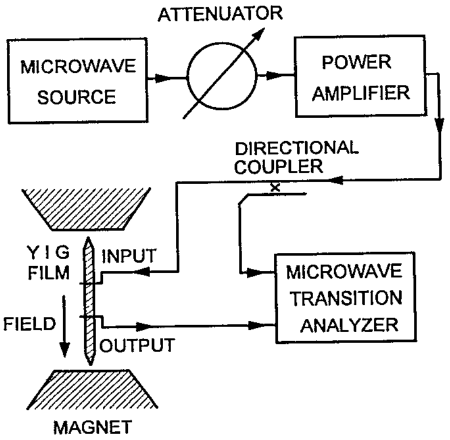

FIG. 4. Block diagram of the microwave measurement system.

A block diagram of the overall experimental setup is shown in Fig. 4. The microwave source consists of three devices: a synthesized sweep generator, a solid-state microwave switch, and a pulse generator. The cw microwave signal is provided by a Hewlett-Packard (HP) model HP83640A synthesized sweeper. The cw signal is then converted into rectangular microwave pulses, as needed, by means of a fast GaAs field-effect-transistor switch driven by an HP8082A pulse generator. The microwave-pulse rise times were below 1 ns. Microwave pulses with widths as narrow as 3 ns are possible. A precision variable attenuator and a traveling-wave-tube power amplifier are used to control the input-pulse power to the MSW transducer structure. The maximum peak power available at the input port to the transducer structure is about 3.5 W. The long narrow YIG film is shown in the gap of the iron yoke electromagnet with the long side parallel to the applied field. The output pulses from the transducer structure and an input reference signal taken from a directional coupler are sent into two separate channels of an HP71500A microwave transition analyzer. The analyzer can be operated either in the frequency domain as a network analyzer or in the time domain as a fast digital sampling oscilloscope. The data from the analyzer are collected by a computer through a standard IEEE-488 interface bus.

B. Linear magnetostatic-wave propagation characteristics

In addition to the FMR measurements to characterize the YIG film, cw and pulse measurements were also carried out with the transducer structure under low-power conditions to define experimentally the linear magnetostatic-wave propagation characteristics for the film. Specifically, these measurements were of (1) the cw transmission-loss profile for the transducer structure across the MSBVW passband and (2) the MSBVW pulse propagation time vs frequency for pulse propagation between the two microstrip transducers.

Figure 5 shows an experimental cw transmission loss vs frequency profile for the structure in the MSBVW configuration with an input power level of 1 mW and an

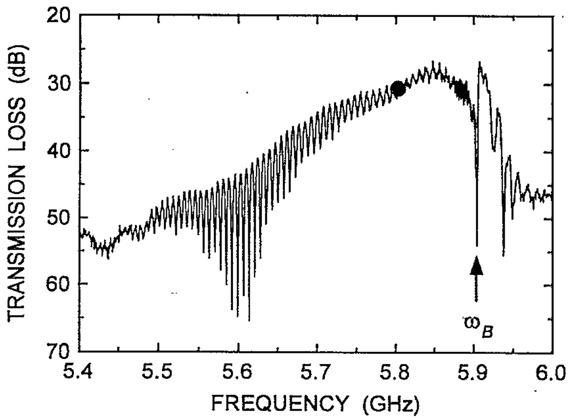

FIG. 5. Low-power transmission loss vs measurement frequency for the YIG-film transducer structure of Fig. 3 in the MSBVW configuration. The film thickness was 7.2 μm and the external applied field was 1343 Oe. The input cw microwave power was 1 mW. The arrow marks the upper edge of the MSBVW frequency passband at $\omega_B = 5.9$ GHz. The filled circle on the loss curve at 5.8 GHz marks the operating point for the soliton experiments.

applied static field H_{app} of 1343 Oe. This is the field needed to position the upper cutoff of the MSBVW passband, shown by the arrow in Fig. 5, at 5.9 GHz. This cutoff frequency corresponds to the $\omega_k = \omega_B$ point in Fig. 1(b). The additional signals just above 5.9 GHz are due to spurious surface-wave effects.[44] From Sec. II, recall that a field $H = 1407$ Oe was needed to position the calculated ω_B at 5.900 GHz. The field difference, $H - H_{\text{app}} = 64$ Oe, is taken as the effective anisotropy field for the in-plane-magnetized YIG film. Additional FMR measurements showed that this anisotropy field is independent of the in-plane-field orientation to within ±2 Oe. Such a field is consistent with the known magnetocrystalline anisotropy for YIG.

The transmission-loss curve in Fig. 5 shows that, as one moves from $\omega_k = \omega_B$ to lower frequencies within the passband, the transmission loss increases dramatically. Below about 5.4–5.5 GHz, the transmission loss levels off at about 50–55 dB due to coupling losses. Recall that the lower passband limit at $\omega_k = \omega_H$ is at 3.940 GHz. The useful frequency range from 5.9 down to 5.5 GHz corresponds to only the upper 20% of the passband. The variation in transmission loss as the frequency decreases from ω_B is due to (a) the change in coupling between the microstrip transducers and the film as the MSBVW wave number k increases, and (b) the increase in signal decay due to relaxation as the MSBVW wave-packet group velocity v_g decreases and the propagation time increases.

Given the MSBVW passband cutoff at 5.900 GHz for a 1343-Oe applied field, the reasoning for the previously indicated soliton operating point at $\omega = 5.8$ GHz, shown by the filled circles on the dispersion curve of Fig. 1(b) and the loss curve in Fig. 5, is now clear. First, it is important to operate reasonably close to the $k = 0$ band edge at $\omega_k = \omega_B$ in order to have strong MSW-transducer coupling and a large group velocity. Second, with the anticipated need for *short* microwave pulses on the order of 10 ns or so in width, one needs to have an operating point which is somewhat below ω_B in order to keep the spectral width of the wave packet within the MSW passband. Pulse widths of 10 ns correspond to a spectral half-width in frequency of 100 MHz. The soliton operating point was positioned, therefore, at 5.8 GHz. As already noted, this operating point corresponds to a MSBVW wave number k of about 200 rad/cm. From Fig. 5, the peak in transmission at 5.85 GHz indicates, therefore, that the coupling is strongest at $k \approx 100$ rad/cm, or a wavelength of 600 μm. Recall that the width of the microstrip transducer is 50 μm.

As discussed above, the FMR spectra indicated unpinned surface spins. Transmission loss vs frequency profiles similar to the curve in Fig. 5 but for the MSSW or MSFVW configurations can also be used to check the extent of surface spin pinning. The presence of pinning causes the appearance of regular notches in the MSSW or MSFVW profiles, while smooth profiles indicate no pinning.[12,15,45] Transmission loss vs frequency profile measurements for the MSFVW configuration were made to verify the lack of pinning inferred from the FMR measurements. As one would expect from the dispersion curve in Fig. 1(c), these profiles showed a low-frequency band edge near $\omega_H = 3.94$ GHz, and a rapid decrease in transmission as the frequency was increased. The profiles showed none of the pronounced notch structure connected with pinning.

Low-power MSBVW propagation time measurements were also made. For the 4-mm transducer separation and the range of group velocities evident from Fig. 1(b), $|v_g| \approx 3\text{–}4 \times 10^6$ cm/s, propagation times in the 100–150-ns range are expected. The basic experiment was to launch short, low-power MME pulses, measure the delayed pulse at the output transducer, and determine the propagation time between input and output.[12] Figure 6 shows the results of these measurements, carried out for the same applied field as before, 1343 Oe. The input-pulse width was 12 ns and the input peak power was about 20 mW. Propagation time measurements were possible only over the high-transmission 5.6–5.9-GHz portion of the passband. The filled circles show the measured propagation times. The dotted line represents a straight-line best fit to the data. The solid curve shows calculated propagation time vs frequency, based on the MSBVW dispersion curve of Fig. 1(b). The vertical dashed line at 5.9 GHz denotes the MSBVW band edge at $\omega = \omega_B$. The figure shows fairly good agreement between the data and the theory. The calculated propagation times fall below the data by less than 8% over the range of the measurements. The measured propagation time at the 5.8-GHz soliton operating point is 123.5 ns, corresponding to $|v_g| = 3.24 \times 10^6$ cm/s for the 4-mm separation between the input and output transducers. The slope of the experimental propagation time vs frequency response at the operating point is equal to -1.66×10^{-17} s^2/rad. This corresponds to a dispersion parameter $\omega_k'' = 1.41 \times 10^3$ cm^2/rad s. These empirical $|v_g|$ and ω_k'' values are close to the values from theory.

A series of pulse propagation measurements was also

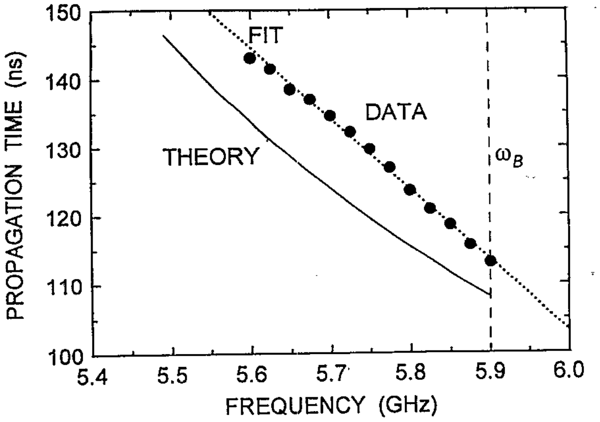

FIG. 6. Propagation time vs measurement frequency for the YIG-film transducer structure for low-power MSBVW pulses. The film thickness was 7.2 μm and the external applied field was 1343 Oe. The microwave input pulses were 12 ns wide and the pulse peak power was about 20 mW. The input and output transducer spacing was 4 mm. The filled circles show the data. The dotted line represents a linear best fit to the data. The solid curve shows the calculated propagation time vs frequency based on the MSBVW dispersion characteristic in Fig. 1(b). The vertical dashed line marks the upper edge of the MSBVW passband at 5.9 GHz. The propagation time at the 5.8-GHz operating point is 124 ns. The slope of the experimental propagation time vs frequency response is close to -100 ns/GHz.

used to determine the MSBVW relaxation rate parameter η applicable to the experiments and modeling. Pulses 50–100 ns in width were launched from the input transducer and then detected at the output transducer, just as in the delay-time measurements. Here, however, the pulse was detected twice, once after its direct pass from input to output, and then again on its return pass after reflection from the end of the film. Both the attenuation and time delay between passes were measured. This type of measurement was done for several different positions of the reflecting edge relative to the pickup transducer. The change in attenuation with pulse separation time was determined to be 65 dB/μs. This attenuation rate converts to a relaxation rate $\eta = 7.5\times10^6$ rad/s. As already indicated, this value of η is a factor of 2–3 greater than one would expect from the intrinsic microwave losses in YIG at 5.8 GHz. This increase is attributed to the additional MSBVW propagation losses due to interactions with the GGG substrate.[37]

C. Summary of parameters

The various parameters discussed above are listed in Tables I and II. Where appropriate, the units for frequency and wave number are taken to include explicitly the 2π rad/cycle factor, with frequency parameters in rad/s and wave numbers in rad/cm. Numerical values of parameters have been rounded to represent nominal values. Table I lists parameters for the YIG film, the transducer structure, and the MSBVW signals at the 5.8-GHz operating point defined above. Table II lists characteristic times, critical $T_0^2|u_0|^2$ products, and $|u_0|^2$ thresholds for soliton generation and observation. For the results of the next two sections, initial pulse widths, denoted by T_0, will generally be on the scale of tens of nanoseconds and power amplitudes, denoted by $|u_0|^2$, will be in the range $5-100\times10^{-4}$. Table II shows T_0 and other characteristic time values in ns and $|u_0|^2$ values in units of 10^{-4}.

IV. EXPERIMENTAL RESULTS ON MSBVW MME SOLITONS

The envelope-soliton experiments were performed in the time domain. The procedure was similar to that used

TABLE I. List of parameters for the YIG film, the MSBVW signals, and the transducer structure.

Parameter name	Parameter symbol	Value
Film thickness	S	7.2 μm
Transducer separation	L	4 mm
Saturation induction	$4\pi M_s$	1750 G
Gyromagnetic ratio	γ	2.8 GHz/kOe 1.76×10^7 rad s^{-1} Oe^{-1}
Net internal static field	H	1407 Oe
Applied static field	H_{app}	1343 Oe
Effective anisotropy field	H_A	64 Oe
MSBVW band upper cutoff frequency	ω_B	5.90 GHz 3.708×10^{10} rad/s
Operating frequency	ω	5.80 GHz 3.644×10^{10} rad/s
MSW band lower cutoff frequency	ω_H	3.94 GHz 2.476×10^{10} rad/s
MSBVW group velocity	$\lvert v_g\rvert$	3.2×10^6 cm/s
MSBVW dispersion coefficient	$\omega_k''=\partial^2\omega_k/\partial k^2$	1.4×10^3 cm^2/rad s
FMR relaxation rate	η	7.5×10^6 rad/s
Nonlinear response coefficient	$N=\partial\omega_B/\partial\lvert u\rvert^2$	-7.4×10^9 rad/s

TABLE II. Characteristic times and parameter limits for solitons.

Parameter name	Parameter symbol	Value
Relaxation time	T_r	133 ns
Dispersion time	T_d	$7.4[T_0\ (\text{ns})]^2$ (ns)
Nonlinear response time	T_n	$4200/[\|u_0\|^2\times 10^4]$ (ns)
Propagation time	T_p	124 ns
Critical $T_0^2\|u_0\|^2$ products for one-, two-, and three-soliton formation	$[T_0^2\|u_0\|^2\times 10^4]_{\text{crit-1}}$	450 ns^2
	$[T_0^2\|u_0\|^2\times 10^4]_{\text{crit-2}}$	4000 ns^2
	$[T_0^2\|u_0\|^2\times 10^4]_{\text{crit-3}}$	11 200 ns^2
Relaxation-time-based soft threshold for $\|u_0\|^2$	$\|u_0\|^2_{rn}\times 10^4$	32
Propagation-time-based soft threshold for $\|u_0\|^2$	$\|u_0\|^2_{pn}\times 10^4$	34

for the low-power propagation time measurements discussed above. Here, however, the focus was on the evolution in shape and peak power for the output pulses as a function of input power level and input-pulse width. At low power and for very short input pulses, the output response was always more or less linear. At higher power, however, the output pulses showed characteristics associated with solitons. These characteristics include a steepening and narrowing of the output pulses, the appearance of output pulses with multiple peaks, and a small change in the propagation velocity with power. As will be evident from the specific results presented below, these data provide important insights about envelope-soliton formation and evolution. Two different series of profile and peak power measurements were performed, one in which the input pulse width was held constant and the input pulse power was changed, and one in which the power was held constant and the pulse width was changed. The results presented below represent a small sample of the many series of profiles which were measured.

A. Experiments for constant input pulse width

Figure 7 shows a series of input and output power profiles for fixed input-pulse width and increasing power. The pulse width was held constant at 13 ns. Traces (a)–(d) show profiles for input powers of 0.3, 1.5, 2.0, and 3.0 W, respectively. Note that the power scales for the input pulses are in W, while the power scales for the output pulses are in mW.

For input-pulse powers in the 0.3-W range, as represented by trace (a) in Fig. 7, the output pulses scale linearly, more or less, with the input. For trace (a), the input power $P_{\text{in}}=0.3$ W maps to a peak output power $P_{\text{out}}=0.35$ mW, for a $P_{\text{out}}/P_{\text{in}}$ ratio of 0.0012. At $P_{\text{in}}=1.5$ W, trace (b) shows the beginning of a trend of steepening and narrowing of the output-pulse profile. Here, the P_{out} value has increased to 2.5 mW, the $P_{\text{out}}/P_{\text{in}}$ ratio has increased to 0.0016, and the output profile is somewhat narrower than for trace (a). This narrowing trend is continued in trace (c), for $P_{\text{in}}=2.0$ W. The large peak in the output profile for trace (c) has narrowed significantly and there is the appearance of a second, smaller peak as well. Note, however, that for trace (c) the peak power $P_{\text{out}}/P_{\text{in}}$ ratio is close to 0.0017, about the same as for (b). Trace (d) is for an input power of 3.0 W. Here, $P_{\text{out}}/P_{\text{in}}$ has dropped back to 0.0007 and the output profile shows two distinct peaks.

The narrowing and steepening effect, the leveling off in $P_{\text{out}}/P_{\text{in}}$, and the appearance of multiple output pulses indicate the formation of MME solitons. These specific results for $T_0=13$ ns indicate that one first sees single-soliton pulses for input power levels in the 1-W range and that multiple solitons are generated above 2 W. It is important to realize, however, that the interpretation of the

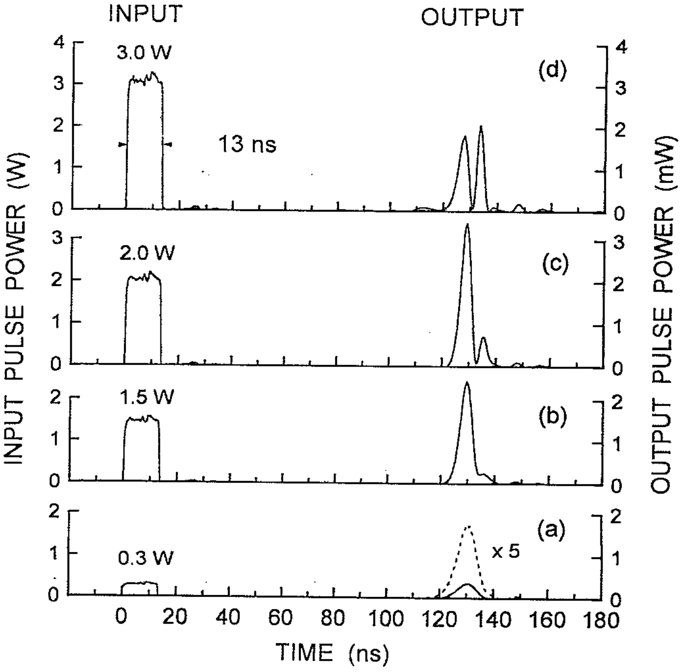

FIG. 7. Input and output profiles of detected power vs time for the YIG-film transducer structure of Fig. 3 in the MSBVW configuration for the four different input power levels indicated. The film thickness was 7.2 μm and the external applied field was 1343 Oe. The carrier frequency was 5.8 GHz and the input-pulse width was held constant at 13 ns. The dotted curve for output profile (a) shows the pulse with the vertical response expanded by a factor of 5.

output-pulse evolution with increasing power shown in Fig. 7 is *complicated* by the fact that the nonlinear response time T_n is *decreasing* as the input-pulse power level is increased. The right-hand profiles for (b) and (c) show soliton pulses progressively closer to the end of their formation process. This point, along with additional characteristic time considerations will be examined in more detail at the end of this section.

Experimental results on the nonlinear dependence of the output-pulse peak power on the input power were reported by De Gasperis, Marcelli, and Miccoli[19,20] and taken as evidence for MSFVW MME soliton propagation in perpendicularly magnetized YIG films. In their experiment, the output peak power was observed to increase nonlinearly with the input-pulse power above a certain threshold. This nonlinear increase in P_{out} relative to P_{in} was attributed to a decrease in the losses associated with soliton pulses above some threshold input power. As will be evident from the results given below, this initial increase is only part of the picture. The initial nonlinear increase in $P_{\text{out}}/P_{\text{in}}$ is followed by a rapid *decrease* in $P_{\text{out}}/P_{\text{in}}$ to values below the linear response extrapolation.

Figure 8 shows results of output peak power P_{out} vs input-pulse power P_{in}, obtained under the same conditions as for Fig. 7. The data are shown by filled circles connected by a smooth curve. For input-pulse power levels under about 0.2 W, indicated by the small arrow, the output peak power increases linearly with the input peak power. For reference, this linear response is shown in Fig. 8 by the dashed line extended across the entire graph. For reasons which will be made clear shortly, a dotted line representing the effect of decay at twice the linear rate is also shown.

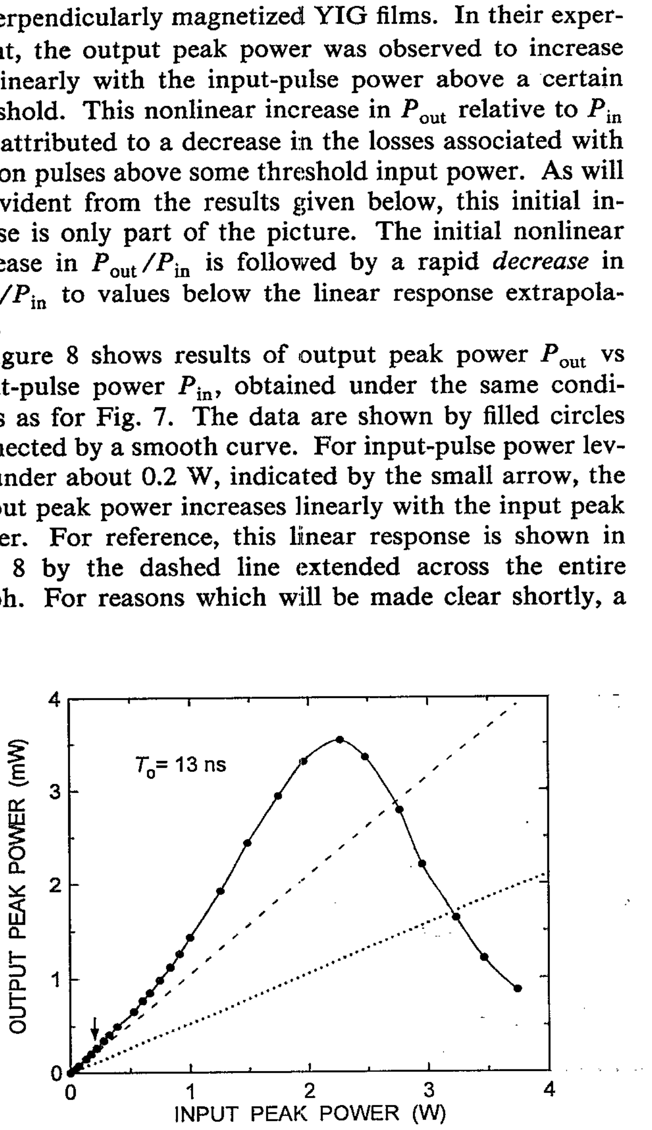

FIG. 8. Measurements of output peak power vs input-pulse peak power for a series of pulse propagation experiments with the YIG-film transducer structure of Fig. 3 in the MSBVW configuration and with the input-pulse width held constant at 13 ns. The film thickness was 7.2 μm and the external applied field was 1343 Oe. The carrier frequency was 5.8 GHz. The filled circle data points are connected by a smooth curve. The dashed line indicates the linear dependence extrapolated from low power. The dotted line indicates the linear response if the decay rate were doubled.

The data in Fig. 8 show that as the input-pulse power increases above 0.2 W or so, the output peak power deviates from the linear response and increases rapidly. This initial nonlinear increase for MSBVW solitons is consistent with the experimental results of De Gasperis, Marcelli, and Miccoli[19,20] for MSFVW solitons. The mechanism for this increase, however, is not related to the elimination of loss. Rather, from the results in Fig. 7, the increase is connected with the pulse narrowing and steepening associated with soliton formation.

The initial nonlinear response in P_{out} relative to P_{in} does not continue for all powers above threshold. In Fig. 8, the output peak power reaches its maximum point when the input power is at about 2.3 W. For higher input power levels, the output peak power decreases and drops to values well below the linear-response level. Just as the increase in output peak power in the 0.2–1-W range can be connected to the pulse steepening and narrowing associated with the initial stages of single-soliton formation and the decrease in T_n with increasing power, the peak and subsequent decrease in P_{out} can be attributed to the realization of fully formed single solitons as T_n falls below T_p and multiple-soliton processes come into play. If one assumes that the peak at $P_{\text{in}}=2.3$ W corresponds to the point at which $T_n=T_p$ is satisfied, this immediately establishes a power scaling factor between P_{in} and $|u_0|^2\times10^4$. The $T_n=T_p$ condition corresponds to $|u_0|^2\times10^4=|u_0|^2_{pn}\times10^4=34$. The corresponding power scaling factor is given by $|u_0|^2\times10^4/P_{\text{in}}=15\ \text{W}^{-1}$.

A power scaling factor of 15 W^{-1}, moreover, applied to the initial onset of nonlinearity at $P_{\text{in}}\approx0.2$ W, implies a single-soliton $T_0^2|u_0|^2\times10^4$ critical product of about 500 ns^2. This value is quite close to the theoretical single-soliton $[T_0^2|u_0|^2\times10^4]_{\text{crit-1}}$ value of 450 ns^2 in Table II. This power scaling factor, $|u_0|^2\times10^4/P_{\text{in}}=15\ \text{W}^{-1}$, will be the basis of the connections with theory discussed below.

As an alternative, it might appear reasonable to associate the peak in P_{out} in Fig. 8 with the condition for single-soliton formation, determined from $T_n\approx T_d$, Eq. (14) with $n=1$, and expressed as $[T_0^2|u_0|^2\times10^4]_{\text{crit-1}}=450$ ns^2 in Table II. This association, however, leads to an extremely small power scaling factor of 1.1 W^{-1} and an excessively long nonlinear response time $T_n=1600$ ns. It is unlikely that such a long soliton formation time would lead to a peak in P_{out} at the established propagation time of 124 ns.

Just as the peak in P_{out} at $P_{\text{in}}=2.3$ W in Fig. 8 cannot be associated with the condition for single-soliton formation, the decline in P_{out} above $P_{\text{in}}=2.3$ W is not connected simply with multiple-soliton formation, however. For $T_0=13$ ns and the 15-W^{-1} power scaling factor, the two-soliton critical product in Table II implies a two-soliton threshold at $P_{\text{in}}\approx1.6$ W, well below the peak position. The data do show an inflection point at $P_{\text{in}}\approx1.5$ which may reflect the formation of the new soliton. The profiles in Fig. 7 show the second soliton just beginning to appear at $P_{\text{in}}=1.5$ W, growing at 2.0 W, and more or less fully formed at 3.0 W. The corresponding three-soliton threshold is at $P_{\mathrm{in}} \approx 4.4$ W, well beyond the range of the current experiments.

Relaxation and possibly second-order instability effects may be an important consideration in the drop in P_{out} above $P_{\mathrm{in}} \approx 2.3$ W. The relaxation time T_r of 133 ns is very close to the propagation time T_p of 124 ns. It is a well-established experimental and theoretical fact that MME solitons decay at about *twice the rate* of low-power pulses.[46-48] Apart from the steepening and narrowing effect associated with soliton formation, this increased rate of decay would lead to the P_{out} vs P_{in} response indicated by the dotted line in Fig. 8. The present result may well be a result of this increased rate of decay. Once the self-steepening and narrowing effects have taken place and the nonlinear response time has become sufficiently small, the doubled decay rate effect dominates to push P_{out} to levels well below the linear response.

B. Experiments for constant input-pulse power

The second sequence of measurements was for input pulses held at a fixed power of 1.75 W and with varying widths. Traces (a)–(d) in Fig. 9 show input and output profiles for input-pulse widths of 5, 18, 27, and 38 ns, respectively. As for Fig. 7, the power scales for the input pulses are in W, while the power scales for the output pulses are in mW.

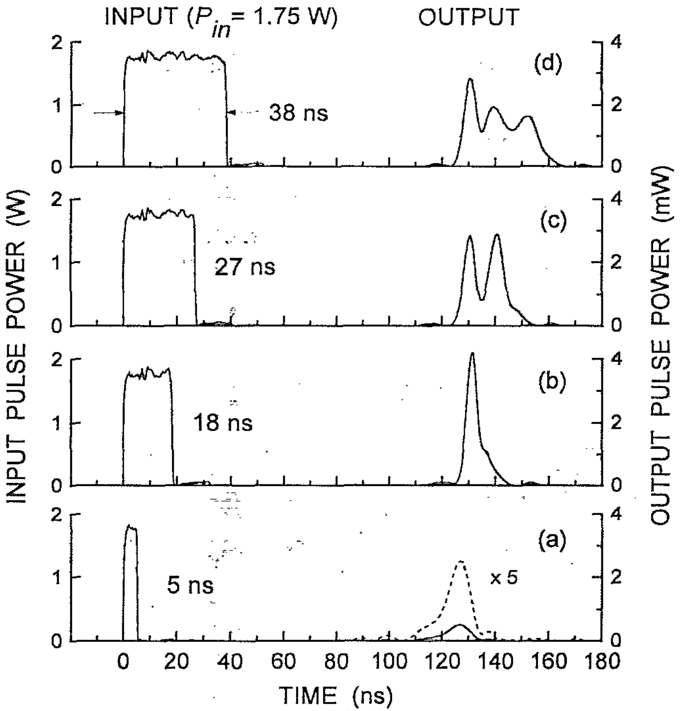

FIG. 9. Input and output profiles of detected power vs time for the YIG-film transducer structure of Fig. 3 in the MSBVW configuration for the four different input-pulse widths indicated. The film thickness was 7.2 μm and the external applied field was 1343 Oe. The carrier frequency was 5.8 GHz and the input-pulse peak power was held constant at 1.75 W. The dotted curve for output profile (a) shows the pulse with the vertical response expanded by a factor of 5.

For trace (a) of Fig. 9, with an input pulse width of 5 ns, one observes a broad and weak output pulse. The broadening is due to the large dispersion for such a narrow input pulse with a wide frequency spectrum of MSBVW signals with different velocities. In trace (b), for an input-pulse width of 18 ns, a well-developed single-soliton output-pulse wave form emerges. The output is significantly narrowed, compared to trace (a). The beginning of a possible second pulse is evident on the trailing edge of the output. Trace (c), for a 27-ns-wide input pulse, shows an output pulse with two peaks. Trace (d), for 38 ns, shows three peaks. These multiple peaks represent, as before, multiple-soliton generation. Note that the output peak powers for (c) and (d) are both about 3 mW.

The sequence of profiles for fixed input power and variable pulse width in Fig. 9 represent a very different physical situation from the Fig. 7 results. Here, fixed power means a fixed value of the nonlinear response time T_n as well. Based on the $|u_0|^2 \times 10^4 / P_{\mathrm{in}} = 15\ \mathrm{W}^{-1}$ power scaling factor discussed above, the value T_n at $P_{\mathrm{in}} = 1.75$ W is 160 ns. This T_n value is still somewhat larger than the 124-ns propagation time, so that the profiles in Fig. 9 still represent only partially evolved solitons. The point, however, is that the T_p / T_n ratio is *constant* for all of the output profiles in Fig. 9 and one is seeing solitons at the *same stage in their evolution* in all the traces.

In parallel with the data in Fig. 8 on output peak power vs input peak power at fixed input-pulse width, measurements were also made of output peak power P_{out} vs input-pulse width T_0 at a fixed input peak power. Representative data are shown in Fig. 10. The input power was held at 1.75 W, the same as for the profiles in Fig. 9. The data show a rather complex response, with an initial increase in P_{out} vs T_0 to a peak, followed by a decrease and a series of oscillations. This response is well correlated with the basic processes of soliton formation already discussed.

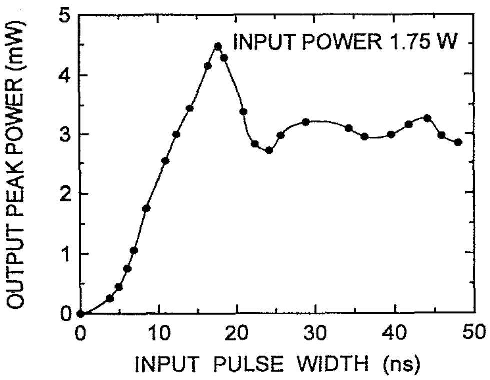

FIG. 10. Measurements of output peak power vs input-pulse width for a series of pulse propagation experiments with the YIG-film transducer structure of Fig. 3 in the MSBVW configuration and with the input-pulse peak power held constant at 1.75 W. The film thickness was 7.2 μm and the external applied field was 1343 Oe. The carrier frequency was 5.8 GHz. The filled circle data points are connected by a smooth curve.

Before examining the data in Fig. 10 in detail, it is useful to establish the basic soliton parameters for the measurement. On the basis of the $|u_0|^2\times10^4/P_{\rm in}=15$ W^{-1} power scaling factor, $P_{\rm in}=1.75$ W corresponds to $|u_0|^2\times10^4=26.25$. From the critical product values in Table II, this power amplitude gives one-, two-, and three-soliton threshold initial pulse widths of 4, 12, and 21 ns, respectively. Note also that $P_{\rm in}=1.75$ W corresponds to a nonlinear response time $T_n=160$ ns, and that the propagation time for the measurements in Fig. 10 is 124 ns.

Return now to consider the data in Fig. 10. The overall increase in output peak power with increasing pulse width in the $T_0=0-18$ ns range comes from the combined effect of dispersion and soliton formation. The data in this range show two features, an increase in slope at $T_0\approx5$ ns and a decrease in slope at $T_0\approx10$ ns. These features can be correlated with soliton effects. At the lowest pulse widths, for $T_0=0-5$ ns or so, the increase in $P_{\rm out}$ with T_0 can be attributed to the effect of dispersion only. In this range, an increase in T_0 narrows the spectral frequency width of the pulse, there is less spreading due to dispersion, and the amplitude of the detected output pulse increases. As the pulse width exceeds the one-soliton threshold of 4 ns, the pulse narrowing and steepening effects associated with soliton formation come into play and $P_{\rm out}$ increases more rapidly with T_0 than below this threshold. This single-soliton break at $T_0=5$ ns is basically the same as the single-soliton break in the data in Fig. 8 at $P_{\rm in}\approx0.2$ W. Both breaks are consistent with the $|u_0|^2\times10^4/P_{\rm in}=15$ W^{-1} power scaling factor obtained from the peak in Fig. 8 and the single-soliton critical product value in Table II.

As T_0 is increased above this initial one-soliton break, multiple-soliton effects appear to come into play. First, the decrease in slope for the Fig. 10 data at $T_0\approx10$ ns or so correlates more or less with the two-soliton threshold of 12 ns. Second, the main peak at $T_0\approx18$ ns matches reasonably well the three-soliton threshold at 21 ns. In making these correlations, it is important to keep in mind that the 124-ns propagation time is still somewhat shorter than the nonlinear response time of 160 ns. The data in Fig. 10, like the data in Fig. 9, represent effects for solitons which are not completely formed.

The above correlations can be extended to the $P_{\rm out}$ vs T_0 response for pulse widths above 20 ns as well. Equation (14), with numerical parameters from Table I, indicates that the spacing in T_0 for multiple-soliton effects should be constant in approximately 8 ns. In line with this prediction, the data in Fig. 10 for T_0 do show a series of oscillations. While the peaks and valleys from the data are not spaced as regularly as one might expect from the theory, the separation times between the peaks or the valleys are in the 12–15-ns range. Such separations are at least in the same range as those obtained from theory.

C. Discussion of pulse profiles

On the basis of the $|u_0|^2\times10^4/P_{\rm in}=15$ W^{-1} power scaling factor and the correlations presented above, a quantitative assessment of the sequences of profiles in Figs. 7 and 9 is possible. The pertinent parameters for the Fig. 7 profiles are listed in Table III. The initial pulse width, pulse propagation time, power scaling factor, and relaxation time are listed at the top of the table. The columns give values for the initial power, the power amplitude, the nonlinear response time, and the $[T_0^2|u_0|^2\times10^4]$ product corresponding to each input-pulse power level. Critical $[T_0^2|u_0|^2\times10^4]$ products for one-, two-, and three-soliton formation are listed at the bottom of the table. The numbers listed in Table III are rounded as appropriate.

One key point from Table III is that, as the power amplitude $|u_0|^2$ increases, the nonlinear response time T_n decreases. For profile set (a) in Fig. 7, T_n is well above the propagation time T_p. This means that, even though the $[T_0^2|u_0|^2\times10^4]$ product is above the critical value of 450 ns^2 for single-soliton formation, the pulse profile detected at 124 ns is just the initial pulse broadened somewhat by dispersion. One would have to wait almost eight times as long to form a soliton at this power level.

The situation for solitons is somewhat better for profile set (b). Here, T_n had dropped to 190 ns. The $[T_0^2|u_0|^2\times10^4]$ product is now at a value of 3800 ns^2, well above the single-soliton critical product and close to the two-soliton critical product value of 4000 ns^2. The actual output profile in Fig. 7 shows one narrow peak and

TABLE III. Pulse profile parameters for Fig. 7 data at fixed initial pulse width.

Initial pulse width $T_0=13$ ns, $|u_0|^2\times10^4/P_{\rm in}$ power scaling factor 15 W^{-1}
Propagation time $T_p=124$ ns, relaxation time $T_r=133$ ns

Profile set	(a)	(b)	(c)	(d)
$P_{\rm in}$ (W)	0.3	1.5	2.0	3.0
$\lvert u_0\rvert^2\times10^4$	4.5	22	30	45
T_n (ns)	940	190	140	94
$[T_0^2\lvert u_0\rvert^2\times10^4]$ product (ns^2)	760	3800	5000	7600
No. of soliton peaks observed	none	one	one plus	two
Critical $[T_0^2\lvert u_0\rvert^2\times10^4]$ products:	One soliton ($n=1$), 450 ns^2 Two solitons ($n=2$), 4000 ns^2 Three solitons ($n=3$), 11 200 ns^2			

the beginnings of a second peak. The power level in this case is large enough to produce the first soliton in time to be detected.

For profile sets (c) and (d), T_n is now close to or somewhat below the propagation time. The corresponding output profiles in Fig. 7 show sharp and fully formed peaks in the maximum peak power range around 3 mW, the same as for profiles (c) and (d) in Fig. 9. Output profile (c) shows one large peak and one smaller peak. Output profile (d) shows two distinct peaks. These profiles are consistent with the $[T_0^2|u_0|^2\times 10^4]$ products listed and the two- and three-soliton critical products at the bottom of the table.

The general trend in Table III is that one observes one less soliton that expected on the basis of the various $[T_0^2|u_0|^2\times 10^4]$ products. While this may be due, in part, to the $T_n > T_p$ effect already noted, this argument applies more to the low-power profile sets (a) and (b) than to sets (c) and (d). It is important, also, to take note of the possible effect of relaxation. In the present setup, the relaxation time of 133 ns is about the same as the 124-ns propagation time. In the case of linear pulses, the exponential pulse decay due to relaxation alone would serve to decrease the initial power amplitude by a factor 0.39 at the output transducer. Such decay amounts to a reduced power amplitude to drive soliton formation. This, in turn, serves to both increase the effective T_n and reduce the effective $[T_0^2|u_0|^2\times 10^4]$ from the values listed in Table III. The net effect, experimentally, is fewer soliton peaks than one would expect from the numbers in the table. The important implication here is that the effect of relaxation is significant for MME solitons. As already indicated, the high-power data in Fig. 8, point to the same conclusion.

The profiles in Fig. 9 may be analyzed in a similar manner. The pertinent parameters for the Fig. 9 profiles are listed in Table IV. The input power, pulse propagation time, power scaling factor, input-pulse power amplitude, nonlinear response time, and relaxation time are listed at the top of the table. The columns give values for the initial pulse widths and the $[T_0^2|u_0|^2\times 10^4]$ product corresponding to each input-pulse width. As for Table III, the critical $[T_0^2|u_0|^2\times 10^4]$ products for one-, two-, and three-soliton formation are listed at the bottom of the table and all numbers are rounded as appropriate.

The key difference here, compared to Table III, is that the power amplitude $|u_0|^2$ is now fixed and the corresponding nonlinear response time T_n is the same for all the profile sets. The 15-W^{-1} power scaling factor gives $|u_0|^2\times 10^4 = 26$ and $T_n = 160$ ns. As already indicated, the nonlinear response time is somewhat greater than the propagation time $T_p = 124$ ns.

As before, the key result in Table IV is in the values for the $[T_0^2|u_0|^2\times 10^4]$ products. The product for profile set (a) is 650 ns^2, which is somewhat above the single-soliton critical product threshold value of 450 ns^2. From the data in Fig. 9, this is insufficient to produce a soliton profile at the pickup transducer 124 ns down line. The lack of an observed soliton peak can be attributed, in part, to the $T_n > T_p$ condition. The more important effect in the present case, however, is probably relaxation. As discussed above, the decay in power amplitude due to relaxation works against soliton formation and should serve to reduce the effective $[T_0^2|u_0|^2\times 10^4]$ product for a given input power amplitude. Conversely, the decay can be viewed as increasing the nonlinear response time T_n. From the data, these combined effects lead to no observed peak for profile set (a).

The $[T_0^2|u_0|^2\times 10^4]$ product for profile set (b) is 8500 ns^2. This is well above the single-soliton threshold, and 124 ns is therefore sufficient to produce a soliton profile at pickup. As evident from Table IV, this product is significantly larger than the two-soliton critical product value of 4100 ns^2. Here, as for profile set (a), the $T_n > T_p$ effect and the power amplitude decay due to relaxation reduce the effective $[T_0^2|u_0|^2\times 10^4]$ to some value below that needed for the observation of two solitons. This basic trend continues for profile sets (c) and (d). The $[T_0^2|u_0|^2\times 10^4]$ product for profile set (c) is 19 100 ns^2, above the three-soliton critical product value of 11 200 ns^2. Yet, the experimental profile shows only two peaks. In this case, the incomplete soliton formation and the effect of relaxation lower the effective $[T_0^2|u_0|^2\times 10^4]$ enough to yield two observed solitons. Profile set (d), for a product of 37 900 ns^2, shows three solitons at the 124-ns propagation time. Here, the reduction is insufficient to drop the effective product below the three-soliton critical

TABLE IV. Pulse profile parameters for Fig. 9 data at fixed initial pulse power.

Initial pulse power $P_{\mathrm{in}} = 1.75$ W, $|u_0|^2\times 10^4/P_{\mathrm{in}}$ power scaling factor 15 W^{-1}
Propagation time $T_p = 124$ ns, Power amplitude $|u_0|^2\times 10^4 = 26$
Nonlinear response time $T_n = 160$ ns
Relaxation time $T_r = 133$ ns

Profile set	(a)	(b)	(c)	(d)
T_0 (ns)	5	18	27	38
$[T_0^2\vert u_0\vert^2\times 10^4]$ product (ns^2)	650	8500	19 100	37 900
No. of soliton peaks observed	none	one	two	three
Critical $[T_0^2\vert u_0\vert^2\times 10^4]$ products:	One soliton ($n=1$), 450 ns^2 Two solitons ($n=2$), 4000 ns^2 Three solitons ($n=3$), 11 200 ns^2			

product value of 11 200 ns^2 and one still observes three peaks.

V. NUMERICAL MODELING OF MSBVW MME SOLITONS

Section IV presented experimental results on MSBVW pulse profiles and peak power correlations at high power levels. These results show characteristics associated with solitons. The data were qualitatively consistent with theoretical considerations based on various characteristic times for the nonlinear response, pulse propagation, relaxation, and dispersion. The basic theoretical approach to MME solitons has been to model the amplitude response $u(z,t)$ by the so-called nonlinear Schrödinger (NLS) equation.[36,48,49] In closing this paper, pulse profiles are obtained from numerical solutions of the NLS equation for parameters which parallel the experimental situation and the measured profiles in Figs. 7 and 9. Pulse profile modeling was also used to generate a theoretical analog to the P_{out} vs P_{in} curve in Fig. 8 and the P_{out} vs T_0 curve in Fig. 10.

The nonlinear Schrödinger equation in terms of z, t, and the various magnetic parameters already discussed may be written as

$$i\left[\frac{\partial u}{\partial t}+v_g\frac{\partial u}{\partial z}+\eta u\right]+\frac{1}{2}\omega_k''\frac{\partial^2 u}{\partial z^2}-N|u|^2u=0\ . \qquad (17)$$

The general origins of the NLS equation are discussed in Refs. 36, 49, and 50. The first term on the left-hand side of Eq. (17), taken alone, gives damped out dispersionless propagation of a MME wave-packet envelope at a speed v_g. The second term contains the effect of dispersion. When dispersion is present, manifested by a nonzero value of ω_k'' and a corresponding curvature in the ω_k vs k dispersion curve at the operating point of interest, this term leads to a spreading out and falloff in amplitude of the MME wave packet as it propagates. The last term on the left-hand side of Eq. (17) is the nonlinear term. Under certain conditions, already discussed in the above sections, this term can lead to solitons.

Soliton solutions to Eq. (17) were obtained by Hasegawa and Tappert[6] in the context of nonlinear optics. Zakharov and Shabat[34,35] also obtained soliton solutions for a simplified version of the NLS equation. The connections between these solutions and MME solitons have been discussed by numerous authors.[13–18,21–23,36,49] In the present case, the NLS equation was solved numerically by the time-forward finite-difference method with time-dependent boundary conditions to simulate the rectangular microwave input pulses used in the experiments. Numerical parameters applicable to the present experiments were listed in Tables I and II and discussed in Sec. III C. The procedure was similar to that used in Ref. 48. Care was taken to use an optimum space-time grid for the parameters at hand. A total propagation distance of 10 mm was used with a distance step of 0.005 mm and a time step of 0.1 ns. As a validity test, solutions were checked over a range of distance and time steps and compared with standard solutions of the NLS equation in reduced form.[34] The program was also tested by using various limiting-case analytic-solution single-soliton profiles as initial conditions and checking the numerical results against the propagating analytic pulse shapes for both temporal and spatial pulses.

A normalized dynamic magnetization envelope pulse $u_0(z,t)$, of amplitude u_0, temporal width T_0, and launched at $z=0$ and $0<t<T_0$, was used to define initial conditions which simulate a square input pulse. Values of T_0 were chosen to match the experimental values in Figs. 7–10. Values of u_0 were chosen to be consistent with the input peak power values in Figs. 7–9 and the $|u_0|^2\times10^4/P_{\text{in}}=15\ \text{W}^{-1}$ power scaling factor from Sec. IV.

Apart from an output scale factor, profiles of output power amplitude $|u|^2$ vs time are theoretical analogs to the experimental output-pulse power profiles of P_{out} vs t presented in Sec. IV. Calculated profiles of $|u|^2\times10^4$ vs time are shown in Fig. 11. The four profiles on the left side of Fig. 11 are for a fixed input-pulse width at $T_0=13$

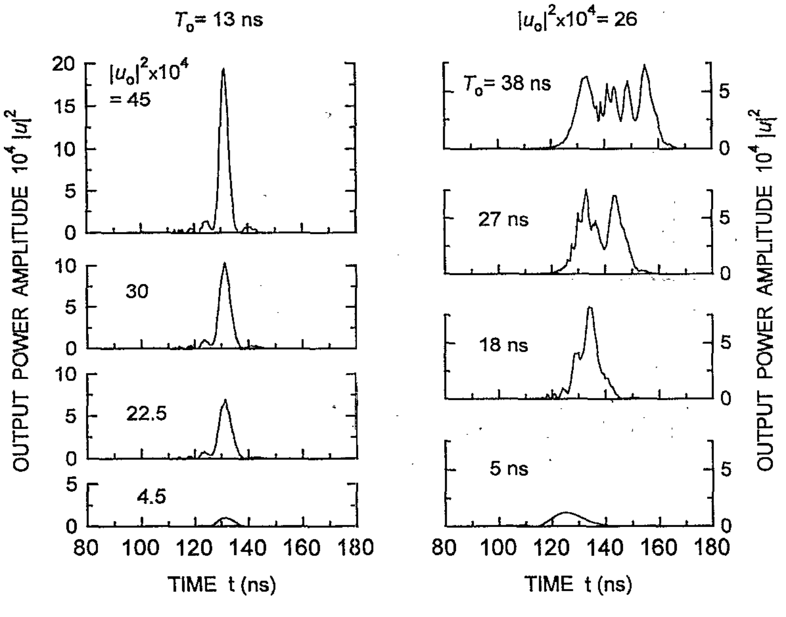

FIG. 11. Calculated profiles of output power amplitude parameter $|u|^2\times10^4$ vs time for various input-pulse widths and input-pulse power amplitudes, based on numerical solutions to the nonlinear Schrödinger equation and with control parameters and initial boundary conditions which match the experiments. For the four traces on the left, the input-pulse width was held constant at $T_0=13$ ns and the input-pulse power amplitude $|u_0|^2$ was increased as indicated. For the four traces on the right, the input-pulse peak power was held at $|u_0|^2\times10^4=26$ and the input-pulse width T_0 was increased as indicated.

ns and input-pulse power amplitudes at $|u_0|^2 \times 10^4$ values of 4.5, 22.5, 30, and 45, respectively. These pulse width and power amplitude values track the input pulses in Fig. 7. The four profiles on the right side of Fig. 11 are for a fixed value of $|u_0|^2 \times 10^4$ at 26 and T_0 values of 5, 18, 27, and 38 ns, respectively. These values track the P_{in} and T_0 values for the experimental profiles in Fig. 9.

The results in Fig. 11 show soliton effects, in the form of pulse narrowing and steepening for the profiles on the left and multiple pulses on the right. Apart from these features, however, the calculated curves bear little resemblance to the experimental output profiles in Figs. 7 and 9. The series of profiles on the left show no hint of multiple peaks as the power amplitude is increased. In addition, the peak power amplitude values simply increase with increasing input power amplitude, and do not show the slightest tendency to level off or decrease in the manner evident from the data. From a careful examination of these curves, the steepening and narrowing process is continuing even at the highest input power amplitude.

The pulse profiles on the right side of Fig. 11 do show a clear evolution from no solitons at the smallest input-pulse width to one, two, and then four peaks as the width is increased. The output peak power amplitudes do appear to level off with soliton formation. The actual profiles, however, are quite ragged and bear little quantitative resemblance to the experimental profiles in Fig. 9.

Based on the arguments at the end of Sec. IV concerning the effect of relaxation in reducing the effective power amplitude which leads to the nonlinear response and soliton formation, it is possible that the problem with the profiles is in the use of too low $|u_0|^2$ values for the calculations. In order to investigate this possibility, profiles similar to those in Fig. 11 were obtained for power amplitudes based on two larger values of the $|u_0|^2 \times 10^4 / P_{\text{in}}$ power scaling factor, 25 and 50 W^{-1}. These higher power amplitudes produced no better match with experiment than before.

Figure 12 shows the results of the numerical calculations for the peak output power amplitude $|u|^2_{\max} \times 10^4$ vs (a) peak input power amplitude $|u_0|^2 \times 10^4$ at a fixed pulse width $T_0 = 13$ ns and (b) input-pulse width T_0 for a constant input-pulse power amplitude $|u_0|^2 \times 10^4 = 26$. These values match the experimental situation for Figs. 8 and 10. The dashed line in Fig. 12(a) shows the linear dependence extrapolated from the response for low input power amplitudes. As with the calculated profile comparisons, the curves in Fig. 12 bear some limited qualitative resemblance to the experimental results. From the $|u|^2_{\max} \times 10^4$ vs $|u_0|^2 \times 10^4$ modeling in Fig. 12(a), one obtains a peak output power amplitude which tracks the input and increases more or less linearly up to about $|u_0|^2 \times 10^4 = 10-15$ or so, shows a local maximum relative to the extrapolated linear response at about $|u_0|^2 \times 10^4 = 80-85$ and then a shallow dip at $|u_0|^2 \times 10^4 \approx 125$, and then increases very rapidly. There is no drop below the linear response at any power amplitude level. The position of these features, if one assumes the power scaling factor $|u_0|^2 \times 10^4 / P_{\text{in}} = 15\ \text{W}^{-1}$, is at powers which are a factor of 3–5 greater than one would expect from the data in Fig. 8. There is no quantitative match to the basic shape found experimentally in Fig. 8 or to the scale of response expected from the $|u_0|^2 \times 10^4 / P_{\text{in}} = 15\ \text{W}^{-1}$ power amplitude scaling factor.

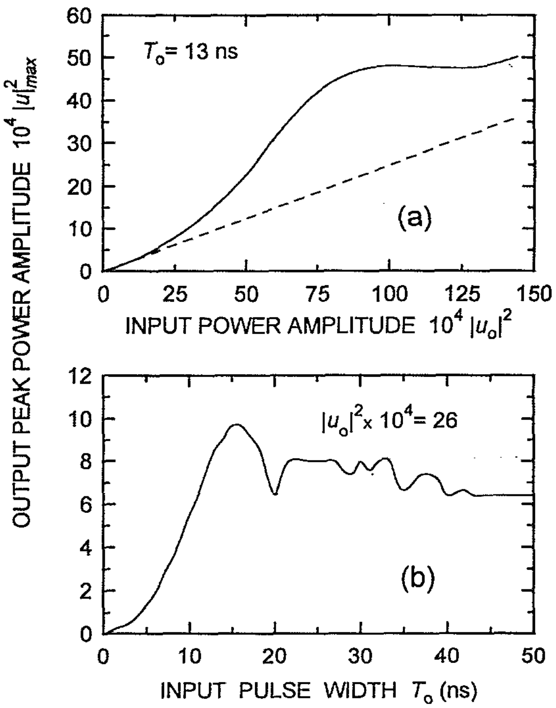

FIG. 12. Peak output-pulse power amplitude $|u|^2_{\max} \times 10^4$ as a function of (a) input-pulse power amplitude $|u_0|^2 \times 10^4$ for a constant input-pulse width held at $T_0 = 13$ ns and (b) input-pulse width T_0 for a constant input-pulse power amplitude $|u_0|^2 \times 10^4 = 26$. The curves were obtained from pulse profiles calculated from the nonlinear Schrödinger equation with control parameters as listed in Table I and initial boundary conditions which simulate the experiments. The dashed line in (a) shows the extrapolated linear response from the calculated response at low power amplitude levels.

The results of the $|u|^2_{\max} \times 10^4$ vs T_0 modeling in Fig. 12(b) bear a somewhat closer resemblance to the corresponding data in Fig. 10. One sees a fairly smooth curve which follows the general shape of the data below $T_0 = 20$ ns. Above $T_0 = 20$ ns, the calculated curve levels off more or less and exhibits some structure as well. The structure, however, appears to show no regular pattern which could be connected with multiple-soliton effects.

It is clear from the above results that the commonly accepted tool for the numerical modeling of MME solitons in thin films, the NLS equation, falls short in accounting for the present experimental results. There are several possible sources for this disagreement. The first involves the one-dimensional nature of Eq. (17). Due to the fact that magnetostatic-backward-volume waves are unstable both in the propagation direction and in the in-plane direction perpendicular to the propagation direction,[36] a NLS equation with two space dimensions might be applicable. Up to now, NLS equations with only one space dimension have been used to model MME solitons. For the present experiments this was justified on the basis of the very narrow films and the resultant guiding of the wave in the nominal propagation direction. It is possible that for 2.5×15 mm^2 films, transverse effects might lead to some modification of the calculated profiles. Such effects, however, are probably small.

There may also be problems in the basic form of Eq. (17). Equation (17) derives from a simple Taylor expansion of the MSW frequency to second-order terms in wave number and first-order terms in power amplitude. Higher-order terms may be needed to model real nonlinear MSW phenomena. Spin-wave instability processes, for example, can lead to additional damping terms which involve $|u|^2$. Such terms may lead to nonlinear damping effects as considered in Ref. 51. Additionally, as discussed in Sec. II B, it may be necessary to examine carefully the relative ranges of power amplitude for second-order spin-wave instability processes as compared to threshold levels for solitons. In any event, it is clear that much more work and new ideas are needed to model MME solitons accurately in magnetic films.

VI. SUMMARY AND CONCLUSION

The above sections have presented a fairly complete set of experiments and analyses on both the linear and the nonlinear response for magnetostatic-backward-volume wave pulses in YIG films. The experiments utilized a magnetostatic-wave transducer structure with a narrow-linewidth single-crystal YIG film. At low power, one obtains well-known MSBVW pulse propagation and attenuation characteristics. At high power, one obtains nonlinear effects in the narrowing and steepening of pulse shapes, the appearance of multiple peaks in the detected pulse, and peak power profiles which show many characteristics associated with envelope solitons. The connection between the experimental results and soliton processes is then considered in terms of various characteristic times for linear and nonlinear MSW wave packets. Good consistency is obtained. Finally, numerical modeling based on the nonlinear Schrödinger equation, parameters which accurately represent the experimental configuration and YIG film, and initial conditions which realistically simulate the experiments, is used to calculate actual profiles and peak power amplitude response curves for comparison with the data. Here, the overall agreement is poor.

The present results provide a clear experimental demonstration of the MME soliton phenomena for MSBVW pulses. The comparisons with theory, however, raise several questions. The first question concerns the large discrepancy between the analytical theory based on the NLS equation and the measurements. The second question concerns the role of damping. Damping plays a clear role in limiting the effectiveness of the nonlinear response in forming solitons. This conclusion is clear from the observed output profiles as well as the peak power response measurements.

One important objective of future work should be to clarify in a quantitative way the connection between damping and soliton formation. In terms of future experiments, it is now clear that a fixed-propagation-length transducer structure allows for only a very limited view of these very different signals at very specific stages of their overall evolution. Work is needed with variable-spacing transducer structures and more detailed spatial profiling of MME solitons by Brillouin light-scattering techniques, inductive pickup, and other means. There also appear to be significant problems in the presently accepted theory for MME solitons in terms of the NLS equation. These problems require immediate study.

ACKNOWLEDGMENTS

The authors gratefully acknowledge Dr. J. D. Adam of the Westinghouse Research and Development Center, Pittsburgh, Pennsylvania for providing the YIG films for the experiment. The authors also thank Dr. B. A. Kalinikos, Dr. A. N. Slavin, Dr. M. J. Ablowitz, Dr. L. F. Mollenauer, Dr. S. A. Nikitov, Dr. P. Kabos, and Dr. A. D. Boardman for helpful discussions. This work was supported in part by the National Science Foundation under Grant No. DMR-8921761 and by the U.S. Army Research Office under Grant No. DAAL03-91-G-0327.

---

[*] On leave of absence from Institute of Electronics, Bulgarian Academy of Sciences, Sofia, Bulgaria.

[1] J. S. Russell, Trans. R. Soc. Edinburgh **14**, 47 (1840).

[2] A. C. Scott, F. Y. F. Chu, and D. W. McLaughlin, Proc. IEEE **61**, 1443 (1973).

[3] G. L. Lamb, *Elements of Soliton Theory* (Wiley, New York, 1980).

[4] M. J. Ablowitz and H. Segur, *Solitons and the Inverse Scattering Transformation* (SIAM, Philadelphia, 1981).

[5] A. Hasegawa, *Optical Solitons in Fibers*, 2nd ed. (Springer-Verlag, Berlin, 1990).

[6] A. Hasegawa and F. Tappert, Appl. Phys. Lett. **23**, 142 (1973); **23**, 171 (1973).

[7] L. F. Mollenauer, R. H. Stolen, and J. P. Gordon, Phys. Rev. Lett. **45**, 1095 (1980).

[8] L. F. Mollenauer and K. Smith, Opt. Lett. **13**, 675 (1988).

[9] H. A. Haus, IEEE Spectrum **30**, 48 (1993).

[10] G. P. Agrawal, *Nonlinear Fiber Optics* (Academic, Boston, 1989).

[11] See Circuits Syst. Signal Process. **4**, (1-2) (1985), Special issue on magnetostatic waves and applications to signal processing.

[12] J. D. Adam, M. R. Daniel, P. R. Emtage, and S. H. Talisa, in *Physics of Thin Films*, edited by M. H. Francombe and J. L. Vossen (Academic, Boston, 1991), Vol. 15, p. 3, and references therein.

[13] B. A. Kalinikos, N. G. Kovshikov, and A. N. Slavin, Pis'ma Zh. Eksp. Teor. Fiz. **38**, 343 (1983) [JETP Lett. **38**, 413 (1983)].

[14] B. A. Kalinikos, N. G. Kovshikov, and A. N. Slavin, Fiz. Tverd. Tela **27**, 226 (1985) [Sov. Phys. Solid State **27**, 135 (1985)].

[15] B. A. Kalinikos, N. G. Kovshikov, and A. N. Slavin, Zh.

Eksp. Teor. Fiz. **94**, 159 (1988) [Sov. Phys. JETP **67**, 303 (1988)].

[16] B. A. Kalinikos, N. G. Kovshikov, and A. N. Slavin, IEEE Trans. Magn. **26**, 1477 (1990).

[17] B. A. Kalinikos, N. G. Kovshikov, and A. N. Slavin, Phys. Rev. B **42**, 8658 (1990).

[18] B. A. Kalinikos, N. G. Kovshikov, and A. N. Slavin, J. Appl. Phys. **69**, 5712 (1991).

[19] P. De Gasperis, R. Marcelli, and G. Miccoli, Phys. Rev. Lett. **59**, 481 (1987).

[20] P. De Gasperis, R. Marcelli, and G. Miccoli, J. Appl. Phys. **63**, 4136 (1988).

[21] B. A. Kalinikos, N. G. Kovshikov, P. A. Kolodin, and A. N. Slavin, Solid State Commun. **74**, 989 (1990).

[22] B. A. Kalinikos, N. G. Kovshikov, and A. N. Slavin, J. Appl. Phys. **67**, 5633 (1990).

[23] M. Chen, M. A. Tsankov, J. M. Nash, and C. E. Patton, Phys. Rev. Lett. **70**, 1707 (1993).

[24] R. W. Damon and J. R. Eshbach, J. Phys. Chem. Solids **19**, 308 (1961).

[25] See, for example, M. Chen and C. E. Patton, in *Nonlinear Phenomena and Chaos in Magnetic Materials,* edited by P. E. Wigen (World Scientific, Singapore, 1994).

[26] R. W. Damon and H. van de Vaart, J. Appl. Phys. **36**, 3453 (1965).

[27] R. E. De Wames and T. Wolfram, J. Appl. Phys. **41**, 987 (1970).

[28] T. Wolfram and R. E. De Wames, Prog. Surf. Sci. **2**, 233 (1972).

[29] M. Sparks, Phys. Rev. B **1**, 3831 (1970).

[30] B. A. Kalinikos, IEEE Proc. **127**, Pt. H. No. 1, 4 (1980).

[31] B. A. Kalinikos, Izv. Vyssh. Uchebn. Zaved. Fiz. **24**, 42 (1981) [Sov. Phys. J. **24**, 718 (1981)].

[32] C. E. Patton, Phys. Rep. **103**, 251 (1984).

[33] M. J. Lighthill, J. Inst. Math. Its Appl. **1**, 269 (1965).

[34] V. E. Zakharov and A. B. Shabat, Zh. Eksp. Teor. Fiz. **61**, 118 (1971) [Sov. Phys. JETP **34**, 62 (1972)].

[35] V. E. Zakharov and A. B. Shabat, Zh. Eksp. Teor. Fiz. **64**, 1627 (1973) [Sov. Phys. JETP **37**, 823 (1973)].

[36] A. K. Zvezdin and A. F. Popkov, Zh. Eksp. Teor. Fiz. **84**, 606 (1983) [Sov. Phys. JETP **57**, 350 (1983)].

[37] M. Maryško, J. Magn. Magn. Mater. **101**, 159 (1991).

[38] G. Payre, Centre de Recherches Mathématiques, Université de Montréal, Montréal, Technical Report CRM-782, 1978 (unpublished).

[39] H. Suhl, J. Phys. Chem. Solids **1**, 209 (1957).

[40] Y. T. Zhang, C. E. Patton, and G. Srinivasan, J. Appl. Phys. **63**, 5433 (1988).

[41] See C. E. Patton, in *Magnetic Oxides,* edited by D. J. Craik (Wiley, London, 1975).

[42] M. Sparks, *Ferromagnetic Relaxation Theory* (McGraw-Hill, New York, 1964).

[43] RT/duroid® 6010 microwave laminate, Rogers Corp., Chandler, AZ 85226.

[44] M. R. Daniel, J. D. Adam, and T. W. O'Keeffe, in *Proc. 1979 Ultrasonics Symposium,* edited by J. deKlerk and B. R. McAvoy (IEEE, New York, 1979), p. 806.

[45] J. D. Adam, T. W. O'Keefe, and R. W. Patterson, J. Appl. Phys. **50**, 2446 (1979).

[46] Y. Kodama and M. J. Ablowitz, Stud. Appl. Math. **64**, 225 (1981).

[47] B. A. Kalinikos, N. G. Kovshikov, and A. N. Slavin, IEEE Trans. Magn. **28**, 3207 (1992).

[48] M. Chen, J. M. Nash, and C. E. Patton, J. Appl. Phys. **73**, 3906 (1993).

[49] V. P. Lukomskii, Ukr. Fiz. Zh. **23**, 134 (1978).

[50] B. B. Kadomtsev and V. I. Karpman, Usp. Fiz. Nauk **103**, 193 (1971) [Sov. Phys. Usp. **14**, 40 (1971)].

[51] N. R. Pereira and L. Stenflo, Phys. Fluids **20**, 1733 (1977).